Geophysical Research Letters

RESEARCH LETTER
10.1029/2018GL078004

Special Section:
Cassini's Final Year: Science Highlights and Discoveries

Saturn's Ionosphere: Electron Density Altitude Profiles and D-Ring Interaction From The Cassini Grand Finale

L. Z. Hadid[1], M. W. Morooka[1], J.-E. Wahlund[1], A. M. Persoon[2], D. J. Andrews[1], O. Shebanits[3], W. S. Kurth[2], E. Vigren[1], N. J. T. Edberg[1], A. F. Nagy[4], and A. I. Eriksson[1]

[1]Swedish Institute of Space Physics, Uppsala, Sweden, [2]Department of Physics and Astronomy, University of Iowa, Iowa City, IA, USA, [3]Space and Atmospheric Physics, The Blackett Laboratory, Imperial College London, London, UK, [4]Climate and Space Sciences and Engineering, University of Michigan, Ann Arbor, MI, USA

Abstract We present the electron density (n_e) altitude profiles of Saturn's ionosphere at near-equatorial latitudes from all 23 orbits of Cassini's Grand Finale. The data are collected by the Langmuir probe part of the Radio and Plasma Wave Science investigation. A high degree of variability in the electron density profiles is observed. However, organizing them by consecutive altitude ranges revealed clear differences between the southern and northern hemispheres. The n_e profiles are shown to be more variable and connected to the D-ring below 5,000 km in the southern hemisphere compared to the northern hemisphere. This observed variability is explained to be a consequence of an electrodynamic interaction with the D-ring. Moreover, a density altitude profile is constructed for the northern hemisphere indicating the presence of three different ionospheric layers. Similar properties were observed during Cassini's final plunge, where the main ionospheric peak is crossed at ~1,550-km altitude.

Plain Language Summary The Cassini Langmuir probe measured directly the uppermost layer of Saturn's atmosphere, the ionosphere, during its Grand Finale. The observations revealed a layered electron density altitude profile with evidence in the southern hemisphere of an electrodynamic type of interaction with the planet innermost D-ring. Moreover, the main peak of the ionosphere is observed for the first time in the *final plunge* around 1,550 km.

Key Points:
- Cassini RPWS observations during the Grand Finale show an electrodynamic type of interaction between the topside ionosphere and the D-ring in the southern hemisphere
- A layered electron density profile is observed, characterized by at least a diffusive and a chemical equilibrium region
- The main ionospheric peak is observed around 1,550 km in the final plunge

Correspondence to:
L. Z. Hadid,
lina.hadid@irfu.se

Citation:
Hadid, L. Z., Morooka, M. W., Wahlund, J.-E., Persoon, A. M., Andrews, D. J., Shebanits, O., et al. (2019). Saturn's ionosphere: Electron density altitude profiles and D-ring interaction from the Cassini Grand Finale. *Geophysical Research Letters*, *46*, 9362–9369. https://doi.org/10.1029/2018GL078004

Received 21 MAR 2018
Accepted 14 JUN 2018
Accepted article online 26 SEP 2018
Published online 22 AUG 2019

1. Introduction

Prior to the Grand Finale, the final phase of the Cassini mission, no in situ measurements of the Kronian ionosphere had been made. Properties of Saturn's ionosphere were inferred based on three different remote observation methods: radio occultation (Kliore et al., 1980, 2014, 2009; Nagy et al., 2006), radio emission from Saturn electrostatic discharges (Fischer et al., 2011; Kaiser et al., 1984), and millimeter-band observations of protonated molecular hydrogen (H_3^+; O'Donoghue et al., 2013). However, only the radio occultation technique has yielded the altitude structure of the electron density. Pioneer 11 (Kliore et al., 1980) and Voyager 1 and Voyager 2 (Lindal et al., 1985) provided the first vertical structures of Saturn's ionosphere. During the early phase of the Cassini mission, density profiles were inferred for near dusk, dawn, equatorial, middle-, and high-latitude conditions (Kliore et al., 2009; Nagy et al., 2006). These observations have shown a decrease in the average electron densities at low latitude (<20°), with lower densities on the dawnside than duskside, and the presence of variable fine structure below about 2,500-km altitude (relative to the height of their calculated 1-bar pressure surface of Saturn). The assumption of spherical symmetry (along the line of sight) limits the use of radio occultation measurements in studying features of the ionosphere that may be spatially localized, such as the effect of the D-ring on the Kronian ionosphere.

In April 2017, Cassini started its Grand Finale phase executing a series of 23 orbits passing between the planet and its rings, with inclination of 61.7° from the planet's equatorial plane. An illustration of all the proximal perikrones is shown in Figure 1. The distance from the center of Saturn varied from 64,668 km (~1.073 R_s) for the closest orbits to the D-ring to 62,076 km (~1.03 R_s) for the deepest orbits. During the last orbit (Rev 293), known as the final plunge (FP), Cassini dove into the planet's atmosphere, sending data for as long as its thrusters could keep the spacecraft's main antenna pointed at Earth. The Radio and Plasma Waves Science/Langmuir probe (RPWS/LP) instrument on board the spacecraft provided unprecedented

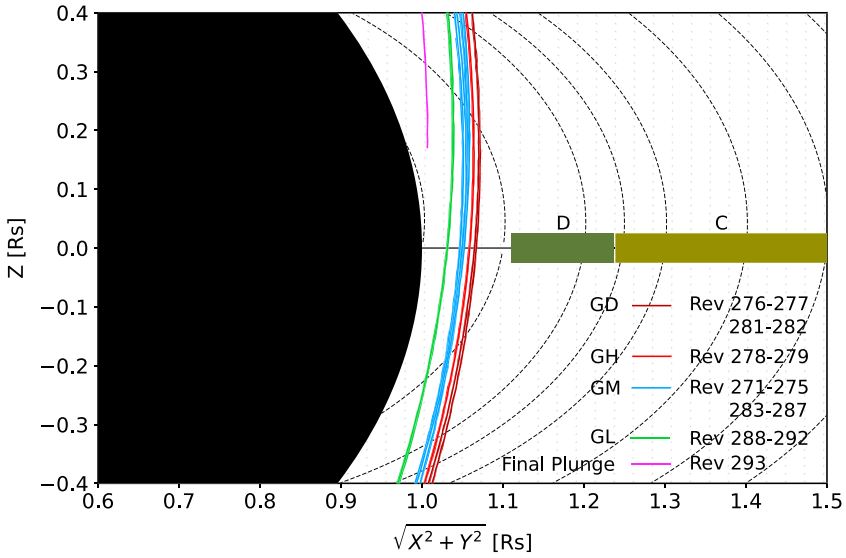

Figure 1. Illustration of the 23 perikrones during the Grand Finale of Cassini passing between Saturn (in black) and the D-ring (dark green). The coordinates are defined as *X* in the solar equatorial plane positive toward the Sun, *Z* northward along the spin axis of the planet, and *Y* completing the right-handed orthogonal set. GD, GH, GM, and GL represent four groups: the closest orbits to the D-ring (GD), the high (GH), middle-latitude (GM), and low-latitude (GL) groups. The magnetic field lines are computed using the internal magnetic field model of Burton et al. (2010).

in situ observations of Saturn's ionosphere. Wahlund et al. (2017) presented the first detection of the topside Kronian ionosphere based on data from the first 11 perikrones [271–282]. They showed a clear variability in the electron number density profiles and evidence for a D-ring interaction at the equatorial plane. Moreover, a north/south asymmetry was shown to be a consequence of the A- and B-rings shadows that reduce the ionization in the southern part of the Kronian atmosphere. In this paper we present the first electron density altitude profile from all proximal orbits. We compare the northern and the southern hemispheres and discuss how the D-ring affects/controls the altitude structure of Saturn's ionosphere.

2. RPWS Experiment Methods

The RPWS investigation provides at least three independent methods to estimate the electron density: two derived from the LP and one estimated from features in the plasma wave spectrum—either a cutoff at the plasma frequency or the upper hybrid frequency band (see Persoon et al., 2019).

2.1. LP Sensor

The first method makes use of the LP sensor, which provides in situ information on the ambient plasma parameters. The probe is a TiN-coated Ti sphere with diameter of 5 cm mounted on a 1.5-m boom (Gurnett et al., 2004; Morooka et al., 2011; Wahlund et al., 2009). It measures the current of the charged particles in two different modes, the voltage sweep mode, and the high-resolution 20-Hz continuous mode. In the sweep mode, the LP samples the total current from the plasma (incoming and outgoing) as a function of an applied bias voltage, U_{bias} (±32 or ±4 V). When applying a positive (or negative) bias potential, the probe will attract electrons and repel ions (or repel electrons and attract ions) from the ambient plasma, and so the resulting current is measured. From the voltage—current characteristics of the LP a number of plasma parameters can be estimated and derived (the spacecraft potential U_{sc}, the electron number density n_e, the electron temperature T_e, the ion density n_i, the ion ram speed v_i, and the average ion mass m_i). More details regarding the derivation of the parameters can be found in Holmberg et al. (2012) and Shebanits et al. (2013, 2016). In the continuous mode, the electron current (I_e) is sampled at a constant bias voltage (+11 V for ±32-V sweep mode and +4 V for ±4-V sweep mode) with 20 samples per second and is proportional to

$$I_e \propto \sqrt{T_e} n_e [1 + \frac{1}{T_e}(U_{sc} + U_{\text{bias}})]. \quad (1)$$

Using T_e and U_{sc} estimates from the voltage sweeps (with lower temporal resolution) and assuming T_e and $U_{sc} \approx$ constant between the sweeps, we can derive n_e with a resolution of 20 Hz (Ågren et al., 2007, 2009).

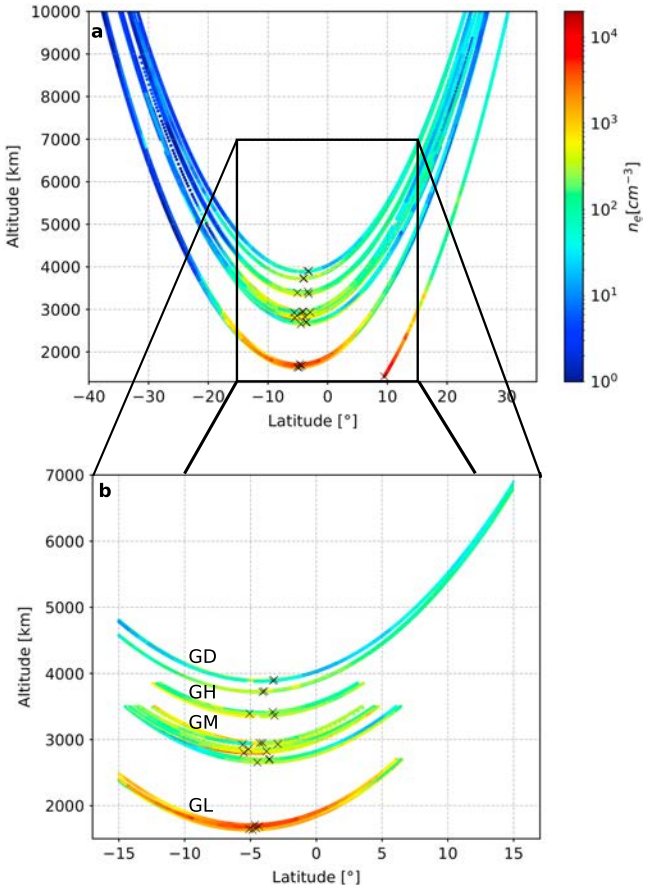

Figure 2. (a) Electron density (color coded) as a function of altitude (h) and latitude (ϕ). (b) Consecutive altitude portions of the density profiles for the latitude range $-15° \leq \phi \leq 15°$ and altitude range $1,200\,\text{km} \leq h \leq 7,000\,\text{km}$. The periapsis on each orbit is marked by a black cross, and GD-GL represent the different altitude groups defined in Figure 1.

2.2. Characteristic Frequencies of Plasma Waves

Another method to estimate n_e is based on observations in the electric field spectra of the sharp upper-frequency cutoff of whistler mode or a line at the upper hybrid frequency (f_{uh}). For the former, the upper cutoff frequency corresponds to the local min(f_{pe}, f_{ce}), where f_{pe} and f_{ce} represent, respectively, the electron plasma and cyclotron frequencies. When the magnetic field is strong, $f_{pe} < f_{ce}$, so n_e is calculated from the cutoff at f_{pe} by using the relation $n_e\,[\text{cm}^{-3}] = (f_{pe}\,[\text{Hz}]/8,980)^2$. When $f_{pe} \gtrsim f_{ce}$, then a band at f_{uh} is apparent. Hence, f_{uh} can be used as it is related to f_{pe} by $f_{uh}^2 = f_{pe}^2 + f_{ce}^2$ and f_{ce} is well known from the magnetometer measurements of $|B|$ since $f_{ce}\,[\text{Hz}] = 28|B|\,[\text{nT}]$ (Gurnett et al., 2005; Persoon et al., 2005, 2019).

3. Observations

3.1. Electron Density Variability

In this work, the electron densities are estimated from the LP high-resolution 20-Hz sampling mode for all the 23 perikrones. At times when LP was partly (Revs 273, 284, 286, and 289) or entirely (Revs 272 and 285) in the wake of the spacecraft, we use the electron densities derived from the upper cutoff frequency of the whistler waves or the f_{uh} line (Persoon et al., 2019), which give identical results, although at lower time resolution (Wahlund et al., 2017). The n_e profiles of the 23 passes are presented in Figure 2a as a function of altitude (h) and geographic latitude (ϕ). The altitudes are computed by considering Saturn as an oblate spheroid with an equatorial radius of 60,268 km and a polar radius of 54,364 km. By convention, the reference altitude is set to a distance of 60,268 km from the center of Saturn in the equatorial plane, which is considered as the 1-bar pressure level. The north-south asymmetry and the large variability in n_e between the orbits (and within single orbit), reported by Wahlund et al. (2017) on the first few perikrones can be seen in Figure 2a. For each orbit the maximum density occurs around the closest approach (*ca*, black crosses) in the southern hemisphere between

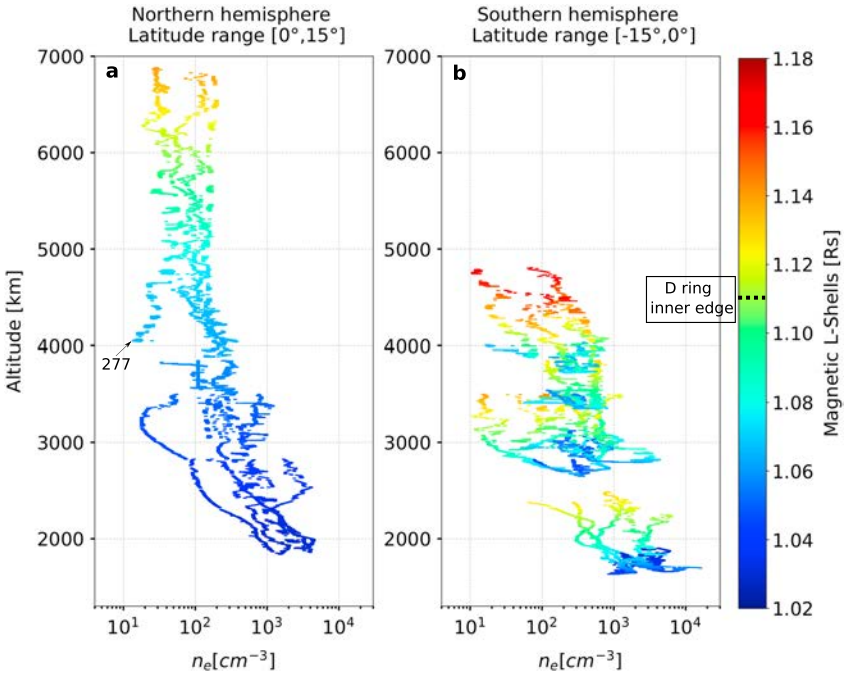

Figure 3. Altitude density profiles of all the proximal orbits (22, all but the final plunge) at equatorial latitudes for the (a) northern and (b) southern hemispheres. The color code signifies the computed magnetic *L*-shells using the internal magnetic field model of Burton et al. (2010).

$\sim -4°$ and $-5°$ with a local time centered around local noon, and a solar zenith angle (SZA) varying between 30° and 35°. The electron number density varies from $\sim$60 cm^{-3} at the highest altitudes ($h > 3,900$ km) up to 2×10^4 cm^{-3} for the lowest altitudes ($h < 2,000$ km). To exclude the effect from the B-ring shadow (Hadid et al., 2018), we limit our analysis to near-equatorial latitudes $-15° \leq \phi \leq 15°$ (Figure 2b). Moreover, in order to study the electron density altitude profile of Saturn's topside ionosphere, we separate, classify, and label the proximal orbits, excluding the FP (Rev 293), into four different groups based on the *ca* altitude: GD, the closest orbits to the D-ring, GH, the high altitude, GM, the midaltitude, and GL, the low altitude ones (Figure 1). Since the FP covers continuously all the altitude ranges, we consider it as a reference and include it in the analysis in section 3.3 where we compare its profile with the average one.

3.2. D-Ring Effect on the Ionospheric Electron Density Structure

To investigate if the rings play a role in structuring the Kronian topside ionosphere, we show in Figure 3 the northern and southern hemisphere h, n_e profiles (excluding for now the FP) as a function of the magnetic *L*-shells (L). In order to get a continuous altitude profile and to confine the study in specific altitude/latitude range, we select, for each group, consecutive altitude ranges as shown in Figure 2b: $1,600 \text{ km} \lesssim h \lesssim 2,830$ km for the deepest altitude group (GL); $2,700 \text{ km} \leq h \leq 3,500$ km for the midaltitude group (GM); $3,350 \text{ km} \leq h \leq 3,850$ km for the high-altitude cases (GH); and $3,750 \text{ km} \leq h \leq 7,000$ km for the closest orbits to the D-ring (GD).

The density increases with decreasing altitude over about 2 orders of magnitude both in the northern and southern hemispheres. However, despite this similarity, clear differences between the two hemispheres can be observed. Contrary to the southern hemisphere (Figure 3b), the altitude profiles in the northern one (Figure 3a) are stable and organized. For $4,000 < h < 7,000$ km the individual density profiles display only small variations and overlap near 4,000 km. Rev 277 is an exception, since it is one of the crossings closest to the D-ring. It has been shown by Wahlund et al. (2017) to be characterized by clear signatures of negative heavy ions/dust grains (>18 amu) near the equatorial plane, probably originating from the D-ring. This was evidenced by the differences in ion and electron densities measured by the Langmuir probe. Below around 4,000 km the n_e profiles start to be highly variable down to 2,000 km, below which they reorganize and become smoother. Furthermore, in the northern hemisphere (Figure 3a) below $\sim$5,000 km, the n_e profiles are related to a narrower and lower range of *L*-shell values ($1.03\,R_s \lesssim L \lesssim 1.08\,R_s$) compared

to the southern hemisphere (Figure 3b), where for each altitude group they vary from ~1.03 R_s up to ~1.18 R_s. The spreading and variability in the electron density profiles are mostly observed in the southern hemisphere at all the altitude ranges whereas they are localized between around [2,200–4,000 km] in the northern hemisphere. Noting that the inner edge of the D-ring is around 66, 900 km (1.11 R_s), implies that up to 5,000 km, the northern density profiles are not connected to magnetic *L*-shells that cross the D-ring, while they do in the southern hemisphere.

3.3. Ionospheric Density Altitude Profile Model

Since the h, n_e variations at equatorial latitudes in the northern hemisphere are not connected to *L*-shells that cross the D-ring (at least not up to 5, 500 km), we assume that they represent *standard* (or typical) profiles of the Kronian topside ionosphere. We show in Figure 4a the averaged h, n_e topside ionospheric profile and model up to 5,500 km. As one can see, it exhibits a layered structure with distinct regions denoted by **P** ($h > 4,000$ km), **D** ($2,200\text{ km} \lesssim h \lesssim 4,000$ km), and **C** ($h < 2,200$ km). The notations **P**, **D**, and **C** refer, respectively, to *Plasmasphere*, *Diffusive*, and *Chemical* discussed in section 4. Region **P** is characterized by near-constant n_e values with respect to altitude before it starts to increase around 4, 500 km, region **D** is highly variable and structured, whereas region **C** is more stable and regular. Ignoring physical processes (e.g., wave phenomena and turbulence), and the variation of gravity and temperature with altitude and assuming diffusive equilibrium, charge neutrality ($n_i = n_e$), thermal equilibrium ($T_i \sim T_e$), and 1-D geometry, we estimate the plasma scale height by fitting with an exponential curve for each of the regions **P, D**, and **C**. We recognize that these are density plots versus altitude and assuming diffusive equilibrium as a function of altitude is questionable but it is useful to obtain such scale height values. We use the following expression:

$$n = n_0 e^{(-h-h_0)/H_{P,D,C}}. \tag{2}$$

Here H is the plasma scale height, the subscript 0 denotes the reference altitude, and P, D, and C corresponds to the different ionospheric regions. Setting the reference altitude to the 1-bar *surface* of Saturn ($h_0 = 0$ km), we find from the following values: $H_P \sim 4,500$ km (consistent with the scale height estimation of the ionosphere in the northern hemisphere by Persoon et al., 2019), $H_D \sim 840$ km, $H_C \sim 260$ km, and $n_{0P} \sim 825\ \mathrm{cm}^{-3}$, $n_{0D} \sim 1.4 \times 10^4\ \mathrm{cm}^{-3}$, $n_{0C} \sim 3.8 \times 10^6\ \mathrm{cm}^{-3}$. The derived plasma scale heights can be compared with a theoretical estimate:

$$H_{\mathrm{theo}} = \frac{2kT_p}{m_i g}, \tag{3}$$

where k is the Boltzmann's constant, T_p is the plasma temperature, m_i is the mean ion mass, and g is the gravitational acceleration at Saturn. Assuming the dominance of H^+ and $T_i \approx T_e \approx 1,160$ K (Wahlund et al., 2017), we obtain $H_{\mathrm{theo}} \approx 1,917$ km. This is significantly larger than the values of 840 and 260 km derived in regions **D** and **C**, respectively, possibly related to the thermal equilibrium assumption we have made ($T_i \approx T_e$) and/or hinting toward a significant component of molecular ions and a mean positive ion mass, in region **D** closer to 2–3 amu (mainly H^+ and H_3^+) and in region **C** $\gtrsim$ 5–10 amu (Morooka et al., 2019; Waite et al., 2018).

In Figure 4b, we present the FP orbit, which covers almost the same altitude range from at least 5,500 km down to 1,300 km. One can clearly relate the three different ionospheric regions highlighted in the averaged profile (Figure 4a). Region **P** where the density looks almost constant with respect to the altitude but increases above ~5,500 km (Persoon et al., 2019), **D** where the profile is characterized by the presence of clear irregular and periodic structures and **C**, where n_e increases exponentially deeper in the ionosphere with a clear ionospheric peak around 1,550 km. The color code corresponds to the magnetic *L*-shell values and shows that region **D** maps well inside the inner edge of the D-ring. The irregular density profiles in the northern hemisphere are therefore not connected to features in the rings. The scale heights are also estimated for this orbit by fitting exponential curves (red lines) using the same formula as before (equation (2). For the FP, the obtained values are $H_{\mathrm{FP},D}$ ~530 km for region **D** and $H_{\mathrm{FP},C}$ ~200 km for region **C** just above the main peak. We note that very similar scale height to $H_{\mathrm{FP},D}$ was estimated by Nagy et al. (2006) to 500 km, for the dusk occultation and more recently by Persoon et al. (2019) to about 540 km, using the characteristic frequencies of the plasma waves. Finally, we fit the observed ionospheric peak, below 2,000 km, with the Chapman model shown by the green curve. The best fit was obtained using the SZA of the FP at those altitudes, which is around 24°, $H = 100$ km, and setting the reference altitude at the ionospheric peak $h_0 = 1,550$ km and the peak density value $n_0 = 1.5 \times 10^4\ \mathrm{cm}^{-3}$. At photochemical equilibrium and with $n_e \approx n_i \approx n_0$, $n_0 \approx \sqrt{q/\alpha}$, where q

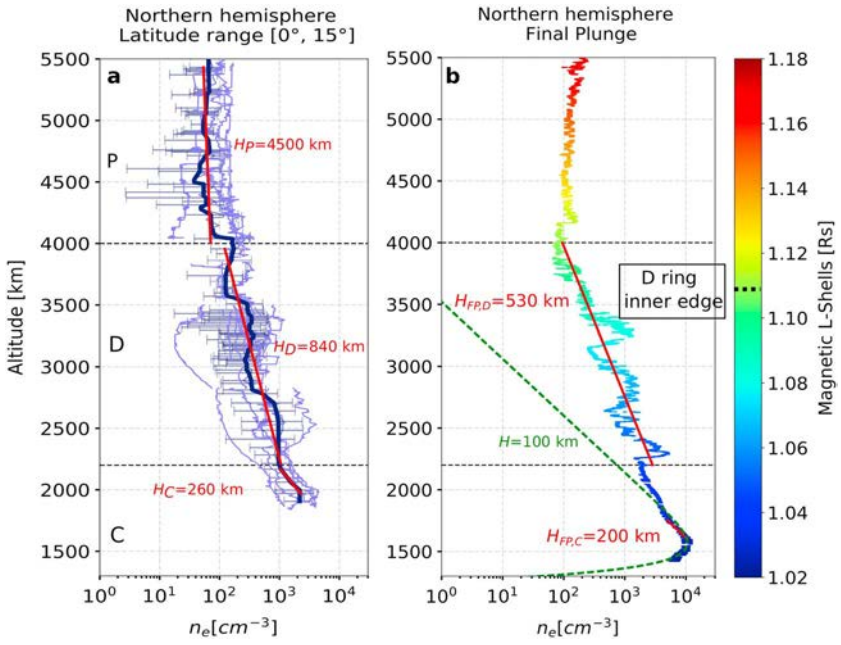

Figure 4. (a) The averaged h, n_e profile (dark blue curve) over all the proximal orbits (purple curves) in the northern hemisphere (except for 293). The error bars represent the standard deviations of the averaged model. (b) The h, n_e profile of the final plunge orbit. The color code shows the corresponding magnetic L-shell values. The Chapman model is represented by the green dashed curve. **P**, **D**, and **C** denote different ionospheric regions delimited by the black dashed lines and the red lines are exponential fitting curves in the different layers. $H_{P,D,C}$ and $H_{FP,D,C}$ represent the estimated scaled heights in the different layers for the northern hemisphere and the *final plunge*, respectively.

is the production rate and α is the effective ion-electron recombination coefficient. Crudely assuming that the peak ionization rate in Saturn's sunlit ionosphere is similar as in Titan's ionosphere ($\sim$30 cm^{-3}/s for similar SZA, see, e.g., Vigren et al., 2013) the relation then gives $\alpha \approx 1.3 \times 10^{-7}$cm^3/s near the peak. This may be viewed as a crude upper limit of α; if electrons are lost partly to charging of macromolecules/grains, the estimated α can to first approximation be corrected by a multiplicative factor n_e/n_i (Vigren et al., 2014).

4. Discussion and Conclusions

Despite the large variability of the electron number densities observed from one orbit to another at equatorial latitudes, the overall altitude profiles showed an increase of n_e toward lower altitude, with a maximum density $> 10^3$ cm^{-3} occurring below 2,000 km (Figure 2) similar to previous radio occultation measurements of the Kronian ionosphere (Kliore et al., 1980, 2009; Lindal et al., 1985; Nagy et al., 2006). However, looking more closely at the northern and the southern hemispheres, the RPWS/LP and the frequency characteristics of the plasma waves when used have revealed a clear north/south asymmetry regarding the structure of the density profiles (Figure 3). The southern hemisphere (Figure 3b) is observed to be much more variable than the northern one regardless of the magnetic L-shell values and is shown to be connected to magnetic L-shells that cross the D-ring ($L \geq 1.11\ R_s$). Moreover, since at those L values, the ionosphere is mainly dominated by H^+ (Wahlund et al., 2017); it implies the dominance of electrodynamical processes via flux tubes, which traverse the electrically conductive D-ring over chemical processes (Waite et al., 2018). In fact, using the RPWS radio measurements, Sulaiman, Kurth, Hospodarsky, et al. (2018) show the presence of clear signatures of whistler waves (classified as auroral hiss and very low frequency saucers) in the southern hemisphere at similar altitudes, directly linked to the planet on field lines connected to the D-ring, hence suggesting as well an electrodynamic coupling with the ring. This highlights the effect of the D-ring interaction on structuring and increasing the variability of the electron density profiles in the topside southern hemisphere. Furthermore, it confirms the role of Saturn's strong magnetic field in facilitating the coupling between the rings and the Kronian ionosphere. It is worth noting that this asymmetry is actually a direct consequence of the northward offset of Saturn's magnetic equator by about 2,700 km (0.036 R_s; Burton et al., 2010).

Thanks to the very high time resolution of the LP 20-Hz mode, the topside ionospheric density profile model constructed in the northern hemisphere (Figure 4a) and the FP event (Figure 4b) highlights the presence

of three different layers, regular (**P** and **C**) and irregular (**D**) ones, characterized by different plasma processes. Layer **P**, above 4,500 km can be interpreted as the inner part of the *plasmasphere* dominated by H^+ with very few collisions and characterized by convection transfer.

Layer **D**, between ~4,000 and ~2,200 km, represents a diffusive equilibrium region, where the electron density decreases exponentially with altitude. We note that since Cassini is crossing field lines rapidly, the estimated scale heights in this layer (840 km and 530 km, Figures 4a and 4b, respectively) are not equivalent to vertical plasma scale heights. Instead, Cassini is sampling the variation in ionospheric densities and temperatures as it traverses the different flux tubes. This could explain the different variations observed in the density profiles consistent with previous radio occultation measurements at similar altitude range (Kliore et al., 2009; Lindal et al., 1985; Nagy et al., 2006). Moreover, it is noteworthy that unlike the southern ionosphere, for this particular altitude range, the observed irregularities present sharp gradients in the electron number density. Furthermore, since the variations are connected to magnetic *L*-shell values $<1.07\ R_s$ implies that they are not associated with field lines that connect to the D-ring (as one can see in Figure 3a). Other than diffusive processes, other physical processes (e.g., turbulence, wave phenomena, plasma instabilities—Rayleigh Taylor or the Perkins instabilities—undamped gravity waves, and wind-induced drifts along the magnetic field lines) could also induce such irregularities. Matcheva et al. (2001) showed at Jupiter, although at much lower altitudes between about 600 and 900 km, that gravity waves are likely to be important in creating steep, multiple density peaks. Moreover, Sulaiman, Kurth, Persoon, et al. (2017) evidence the presence of intense harmonic emissions covering similar altitude range.

Layer **C**, the region below 2,200 km, represents a chemical equilibrium region, dominated by chemical processes. Morooka et al. (2019) observe the dominance of negatively and positively charged heavy cluster ions in this altitude range, and Cravens et al. (2019) interpret it as a nondiffusive layer of heavy molecular ions. Moreover, recently the Ion-Neutral Mass Spectrometer observations implied the presence of organic ions at those low altitudes (Waite et al., 2018), and the densities of positive dust grains measured by the Charge Energy Mass Spectrometer, designed to measure only the positive dust, are shown to be directly proportional to the heavy positive ion population (Mitchell et al., 2018) below 1,700 km. The estimated scale heights in this **C** layer (260 km and 200 km, Figures 4a and 4b, respectively) probably represent the true neutral scale heights. Noting that the profiles in layer **D** are dominated by H^+, and because of the gravity, the density, the mass, and temperature gradients (Morooka et al., 2019), an ambipolar electric field will generate in the plasma within regions **D** and **C**. As a consequence, this would result in the h, n_e variability at this boundary region. This transition from chemical to diffusion dominance is similar to the sub–F_2 region in the terrestrial ionosphere (Schunk & Nagy, 2009).

Last but not the least, during the FP orbit (Figure 4b), the RPWS/LP 20 samples/s have revealed a density peak of $\sim 1.5 \times 10^4\ cm^{-3}$ around 1,550 km, which we interpret as the *main peak* of the Kronian ionosphere. Our observations represent the first detailed in situ measurements of the ionospheric peak of Saturn with high accuracy. They are consistent with previous ionospheric models where the main peak was observed around 1,900 km and a maximum electron densities around $10^4\ cm^{-3}$ (Moore et al., 2006). This is further confirmed by ionospheric photochemical equilibrium models compared to data (Moore et al., 2018).

Acknowledgments
The RPWS/LP instrument on board Cassini is supported by the Swedish National Space Board (SNSB). L. Z. H. acknowledges funding by the Swedish Research Council (Vetenskapsrådet, VR) under the contract 2016-05364. M. W. M. acknowledges funding by the SNSB under contract Dnr 174/15. O. S. acknowledges funding by the Royal Society. N. J. T. E. acknowledges funding by the SNSB under contract Dnr 135/13 and VR under contract 621-2013-4191. The research at the University of Iowa was supported by NASA through contract 1415150 with the Jet Propulsion Laboratory. The research at the University of Michigan was supported by NASA through contract 1416972 with the Jet Propulsion Laboratory. Cassini RPWS data will be available on NASA Planetary Data System: https://pds.jpl.nasa.gov.

References

Ågren, K., Wahlund, J.-E., Garnier, P., Modolo, R., Cui, J., Galand, M., & Muller-Wodarg, I. (2009). On the ionospheric structure of Titan. *Planetary and Space Science*, *57*, 1821–1827. https://doi.org/10.1016/j.pss.2009.04.012

Ågren, K., Wahlund, J.-E., Modolo, R., Lummerzheim, D., Galand, M., Müller-Wodarg, I., et al. (2007). On magnetospheric electron impact ionisation and dynamics in Titan's ram-side and polar ionosphere—A Cassini case study. *Annales Geophysicae*, *25*, 2359–2369. https://doi.org/10.5194/angeo-25-2359-2007

Burton, M. E., Dougherty, M. K., & Russell, C. T. (2010). Saturn's internal planetary magnetic field. *Geophysical Research Letters*, *37*, L24105. https://doi.org/10.1029/2010GL045148

Cravens, T. E., Moore, L., Waite, J. H. Jr, Perryman, R., Perry, M., Wahlund, J.-E., et al. (2019). The ion composition of Saturn's equatorial Ionosphere as observed by Cassini. *Geophysical Research Letters*, *46*. https://doi.org/10.1029/2018GL077868

Fischer, G., Gurnett, D. A., Zarka, P., Moore, L., & Dyudina, U. A. (2011). Peak electron densities in Saturn's ionosphere derived from the low-frequency cutoff of Saturn lightning. *Journal of Geophysical Research*, *116*, A04315. https://doi.org/10.1029/2010JA016187

Gurnett, D. A., Kurth, W. S., Hospodarsky, G. B., Persoon, A. M., Averkamp, T. F., Cecconi, B., et al. (2005). Radio and plasma wave observations at Saturn from Cassini's approach and first orbit. *Science*, *5713*(307), 1255–1259. https://doi.org/10.1126/science.105356

Gurnett, D. A., Kurth, W. S., Kirchner, D. L., Hospodarsky, G. B., Averkamp, T. F., Zarka, P., et al. (2004). The Cassini radio and plasma wave investigation. *Space Science Reviews*, *114*, 395–463. https://doi.org/10.1007/s11214-004-1434-0

Hadid, L. Z., Morooka, M. W., Wahlund, J.-E., Moore, L., Cravens, T. E., Hedman, M. M., et al. (2018). Ring shadowing effects on Saturn's ionosphere: Implications for ring opacity and plasma transport. *Geophysical Research Letters*, *45*, 10,084–10,092. https://doi.org/10.1029/2018GL079150

Holmberg, M. K. G., Wahlund, J.-E., Morooka, M. W., & Persoon, A. M. (2012). Ion densities and velocities in the inner plasma torus of Saturn. *Planetary and Space Science*, *73*(1), 151–160. https://doi.org/10.1016/j.pss.2012.09.016

Kaiser, M. L., Desch, M. D., & Connerney, J. E. P. (1984). Saturn's ionosphere: Inferred electron densities. *Journal of Geophysical Research*, *89*, 2371–2376. https://doi.org/10.1029/JA089iA04p02371

Kliore, A. J., Lindal, G. F., Patel, I. R., Sweetnam, D. N., Hotz, H. B., & Mcdonough, T. R. (1980). Vertical structure of the ionosphere and upper neutral atmosphere of Saturn from the pioneer radio occultation. *Science*, *207*(4429), 446–449. https://doi.org/10.1126/science.207.4429.446

Kliore, A. J., Nagy, A., Asmar, S., Anabtawi, A., Barbinis, E., Fleischman, D., et al. (2014). The ionosphere of Saturn as observed by the Cassini radio science system. *Geophysical Research Letter*, *41*, 5778–5782. https://doi.org/10.1002/2014GL060512

Kliore, A. J., Nagy, A. F., Marouf, E. A., Anabtawi, A., Barbinis, E., Fleischman, D. U., & Kahan, D. S. (2009). Midlatitude and high-latitude electron density profiles in the ionosphere of Saturn obtained by Cassini radio occultation observations. *Journal of Geophysical Research*, *114*(A4), A04315. https://doi.org/10.1029/2008JA013900

Lindal, G. F., Sweetnam, D. N., & Eshleman, V. R. (1985). The atmosphere of Saturn—An analysis of the Voyager radio occultation measurements. *The Astronomical Journal*, *90*, 1136–1146. https://doi.org/10.1086/113820

Matcheva, K. I., Strobel, D. F., & Flasar, F. M. (2001). Interaction of gravity waves with ionospheric plasma: Implications for Jupiter's ionosphere. *Icarus*, *2*(152), 347–365. https://doi.org/10.1006/icar.2001.6631

Mitchell, D. G., Perry, M. E., Westlake, J. H., Kollmann, P., Smith, H. T., et al. (2018). Dust grains fall from Saturn's D-ring into its equatorial upper atmosphere. *Science*, *362*. https://doi.org/10.1126/science.aat2236

Moore, L., Cravens, T. E., Müller-Wodarg, I., Perry, M. E., Waite, J. H. Jr., Perryman, R., et al. (2018). Models of Saturn's equatorial ionosphere based on in situ data from Cassini's Grand Finale. *Geophysical Research Letters*, *45*, 9398–9407. https://doi.org/10.1029/2018GL078162

Moore, L., Nagy, A. F., Kliore, A. J., Müller-Wodarg, I., Richardson, J. D., & Mendillo, M. (2006). Cassini radio occultations of Saturn's ionosphere: Model comparisons using a constant water flux. *Geophysical Research Letters*, *33*, L22202. https://doi.org/10.1029/2006GL027375

Morooka, M. W., Wahlund, J.-E., Eriksson, A. I., Farrell, W. M., Gurnett, D. A., Kurth, W. S., et al. (2011). Dusty plasma in the vicinity of Enceladus. *Journal of Geophysical Research*, *116*(A12), A12221. https://doi.org/10.1029/2011JA017038

Morooka, M. W., Wahlund, J.-E., Hadid, L. Z., Eriksson, A. I., Edberg, N. J. T., Vigren E., et al. (2019). Saturn's dusty ionosphere. *Journal of Geophysical Research: Space Physics*, *124*, 1679–1697. https://doi.org/10.1029/2018JA026154

Nagy, A. F., Kliore, A. J., Marouf, E., French, R., Flasar, M., Rappaport, N. J., et al. (2006). First results from the ionospheric radio occultations of Saturn by the Cassini spacecraft. *Journal of Geophysical Research*, *111*, A06310. https://doi.org/10.1029/2005JA011519

O'Donoghue, J., Stallard, T. S., Melin, H., Jones, G. H., Cowley, S. W. H., Miller, S., et al. (2013). The domination of Saturn's low-latitude ionosphere by ring 'rain'. *Nature Physics*, *496*, 193–195. https://doi.org/10.1038/nature12049

Persoon, A. M., Gurnett, D. A., Kurth, W. S., Hospodarsky, G. B., Groene, J. B., Canu, P., & Dougherty, M. K. (2005). Equatorial electron density measurements in Saturn's inner magnetosphere. *Geophysical Research Letters*, *32*, L23105. https://doi.org/10.1029/2005GL024294

Persoon, A. M., Kurth, W. S., Gurnett, D. A., Groene, J. B., Sulaiman, A. H., Wahlund, J.-E., et al. (2019). Electron density distributions in Saturn's ionosphere. *Geophysical Research Letters*, *46*, 3061–3065. https://doi.org/10.1029/2018GL078020

Schunk, R. W., & Nagy, A. F. (2009). *Ionospheres: Physics, plasma physics, and chemistry* (2nd ed.). Cambridge Atmospheric and Space Science Series. Cambridge: Cambridge University Press.

Shebanits, O., Wahlund, J.-E., Edberg, N. J. T., Crary, F. J., Wellbrock, A., Andrews, D. J., et al. (2016). Ion and aerosol precursor densities in Titan's ionosphere: A multi-instrument case study. *Journal of Geophysical Research: Space Physics*, *121*, 10,075–10,090. https://doi.org/10.1002/2016JA022980

Shebanits, O., Wahlund, J.-E., Mandt, K., Ågren, K., Edberg, N. J. T., & Waite, J. H. (2013). Negative ion densities in the ionosphere of Titan-Cassini RPWS/LP results. *Planetary and Space Science*, *84*, 153–162. https://doi.org/10.1016/j.pss.2013.05.021

Sulaiman, A. H., Kurth, W. S., Hospodarsky, G. B., Averkamp, T. F., Persoon, A. M., Menietti, J. D., et al. (2018). Auroral hiss emissions during Cassini's Grand Finale: Diverse electrodynamic interactions between Saturn and its rings. *Geophysical Research Letters*, *45*, 6782–6789. https://doi.org/10.1029/2018GL077875

Sulaiman, A. H., Kurth, W. S., Persoon, A. M., Menietti, J. D., Farrell, W. M., Ye, S.-Y., & Hadid, L. Z. (2017). Intense harmonic emissions observed in Saturn's ionosphere. *Geophysical Research Letters*, *44*, 12,049–12,056. https://doi.org/10.1002/2017GL076184

Vigren, E., Galand, M., Shebanits, O., Wahlund, J.-E., Geppert, W. D., Lavvas, P., et al. (2014). Increasing positive ion number densities below the peak of ion-electron pair production in Titan's ionosphere. *The Astrophysical Journal*, *786*(1), 69. https://doi.org/10.1088/0004-637X/786/1/6

Vigren, E., Galand, M., Yelle, R. V., Cui, J., Wahlund, J.-E., Ågren, K., et al. (2013). On the thermal electron balance in Titan's sunlit upper atmosphere. *Icarus*, *223*(1), 234–251. https://doi.org/10.1016/j.icarus.2012.12.010

Wahlund, J.-E., André, M., Eriksson, A. I. E., Lundberg, M., Morooka, M. W., Shafiq, M., et al. (2009). Detection of dusty plasma near the E-ring of Saturn. *Planetary and Space Science*, *14*(57), 1795–1806. https://doi.org/10.1016/j.pss.2009.03.011

Wahlund, J-E., Morooka, W. M., Hadid, L. Z., Persoon, A. M., Farrell, W. M., Gurnett, D. A., et al. (2017). In situ measurements of Saturn's ionosphere show that it is dynamic and interacts with the rings. *Science*, *359*, 66–68. https://doi.org/10.1126/science.aao4134

Waite, J. H. Jr., Perryman, R., Perryman, R. S., Perry, M. E., Miller, K. E., Bell, J., Cravens, T. E. (2018). Chemical interactions between Saturn's atmosphere and its rings. *Science*, *362*. https://doi.org/10.1126/science.aat2382